ACS NANO

www.acsnano.org

ARTICLE

Dynamic Lithium Transport Pathway via Crack Formation in Phase-Separating Battery Particles

Chihyun Nam,[¶] Bonho Koo,[¶] Juwon Kim,[¶] Jinkyu Chung, Jaejung Song, Danwon Lee, Sungjae Seo, Munsoo Song, Seyeon Shin, Namdong Kim, Markus Weigand, Jian Wang, and Jongwoo Lim*

Cite This: *ACS Nano* 2025, 19, 9936−9945

Read Online

ACCESS | Metrics & More | Article Recommendations | Supporting Information

ABSTRACT: **Nanoscale cracks within battery particles are ubiquitously induced during battery cycling. Tracking the origin of nanocrack formation and its subsequent propagation remains challenging, although it is crucial for the cycle life and kinetics of batteries. Moreover, it is even more challenging to understand how such nanocracks influence lithium (de)-insertion pathways and local strain fields within battery particles. In this study, we utilized *operando* scanning transmission X-ray microscopy on individual $LiFePO_4$ (LFP) particles to visualize the relationship between lithium (de)-insertion pathways and crack formation and propagation. We first demonstrate the generation mechanism of nanocracks occurs when the lithium insertion pathway at the edge of fresh LFP particles induces strong tensile stress in the middle of the particle. Then, we directly observe the nanocrack propagation mechanism, where the freshly exposed surface near the crack activates a fast lithium (de)insertion pathway, completely altering the internal stress fields near the nanocrack. Once the nanocrack transforms the dynamic lithium pathway and distribution, the delithiation process induces crack-opening tensile stress, while the lithiation process generates crack-closing compressive stress. 3D phase-field simulations support these observations, showing how dynamic lithium distribution shapes stress fields. Our findings reveal a recursive chemo-mechanical loop involving lithium (de)insertion pathways, internal stress fields, and crack development.**

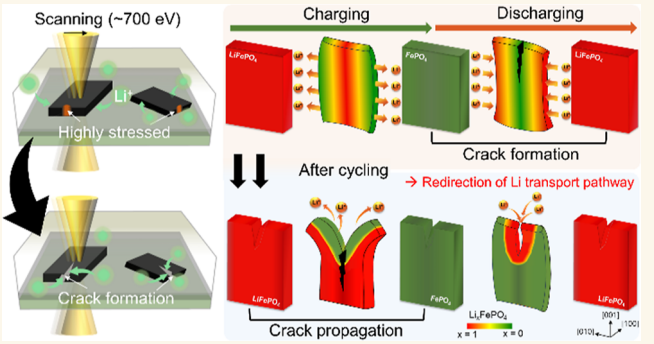

KEYWORDS: *operando soft X-ray imaging, phase separating material, lithium transport pathway, nanoscale crack formation, 3D phase field simulation*

The transport of lithium (Li) within battery particles, along with the resulting strain and stress during cycling, is a key factor in the chemo-mechanical degradation of lithium-ion batteries (LIBs). The electrochemical process of Li (de)-insertion drives nonequilibrium pathways, often resulting in nonuniform Li distribution within active particles.[1−3] This uneven Li distribution leads to localized volume expansions, generating strains and stresses that accelerate mechanical deformations and ultimately cause crack formation.[4−7] Cracks typically form in regions with significant Li heterogeneity, such as at interfaces between Li-rich and Li-poor regions in phase-separating electrodes.[8,9] Even in solid-solution electrodes, where Li distribution is expected to be relatively uniform under near-equilibrium conditions,[10−13] cracks may still emerge due to dynamic Li heterogeneity induced by the (de)insertion process.[14,15] Therefore, understanding how the distribution of Li concentration evolves and contributes to crack formation during battery operation is essential.[16]

Intraparticle cracks can be broadly categorized into two types: major cracks and minor nanoscale cracks (nanocracks).[4,10,12,17,18] Major cracks delaminate entire sections of the active material from the electrode, leading to a loss of electrical or ionic connections. These are often identified through post-mortem analysis[3] and are typically associated with capacity loss and performance degradation.[19−21] In

Received: November 8, 2024
Revised: February 12, 2025
Accepted: February 18, 2025
Published: March 5, 2025

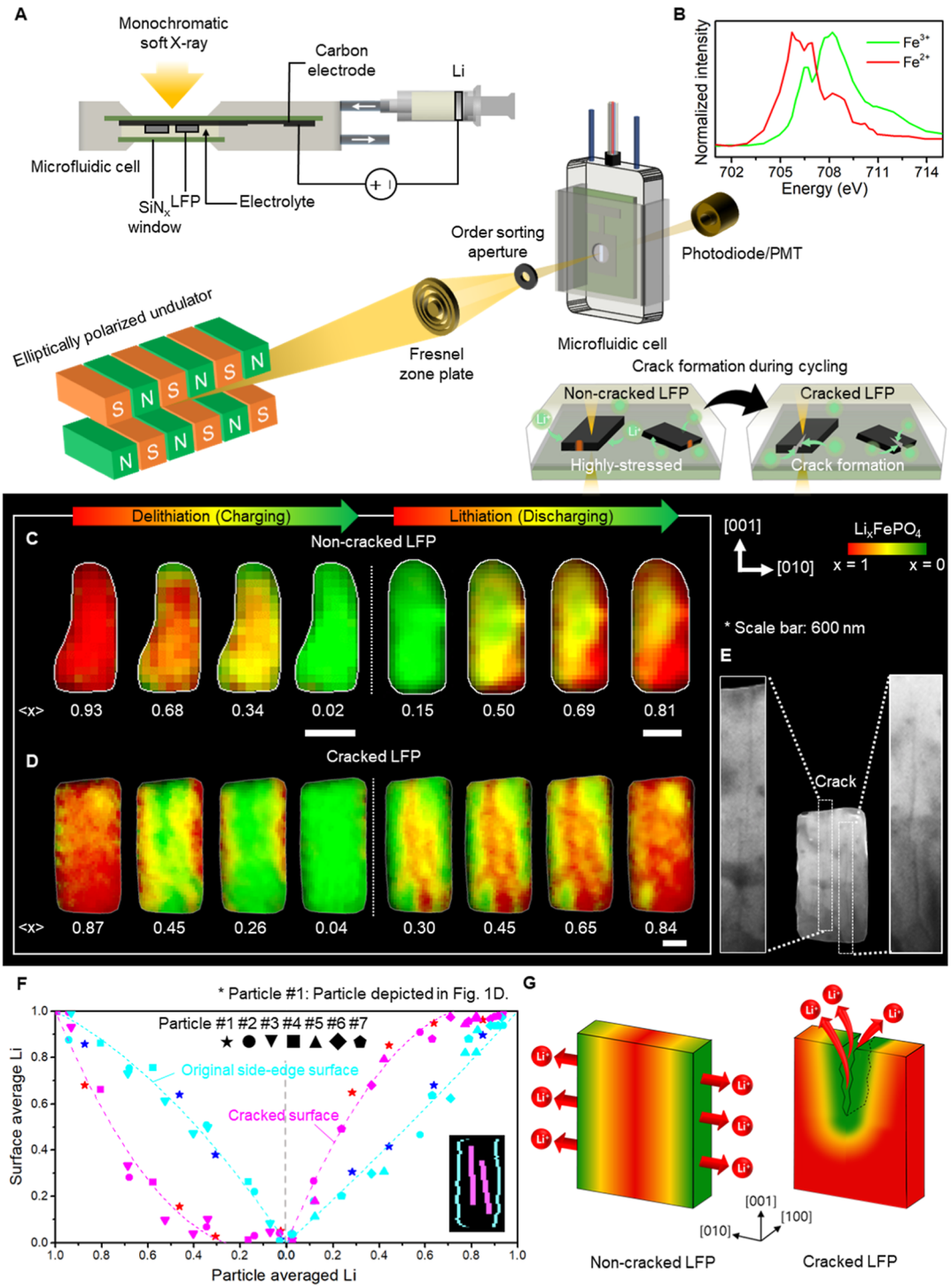

Figure 1. Redirecting Li (de)insertion pathway via internal crack formations. (A) Schematic of an *operando* STXM imaging platform. (B) Fe L_3-edge absorption spectra of as-synthesized ($Li_1Fe^{2+}PO_4$) and fully charged ($Li_0Fe^{3+}PO_4$) [100]-oriented LFP. (C) Li (de)insertion maps captured by *operando* STXM experiments for the noncracked LFP particles during the delithiation and lithiation process. Reproduced with permission from ref 30. Copyright 2023 Royal Society of Chemistry. (D) Observed Li (de)insertion maps for the cracked particle during the delithiation and lithiation process. (E) Corresponding SEM image of cracked LFP particle. (F) Li concentration obtained from the original (010) side-edge surface region (cyan) and the new cracked surface region (magenta) during the cycles. (G) Schematic description of the Li pathway in noncracked (left) and cracked (right) particles.

contrast, minor nanocracks, which maintain electrical and ionic connections, form abundantly during cycling but are harder to detect post-mortem. These newly generated nanocracks create new electrochemically active surfaces,[22−24] altering Li (de)-insertion pathways and influencing internal strain and stress fields. Over time, they may contribute to the formation of larger major cracks. Nanocracks are widespread during battery operation and can unexpectedly modify Li transport pathways compared to the original, as-synthesized particles. However, the mechanisms by which cycling induces nanocracks and

https://doi.org/10.1021/acsnano.4c15960
ACS Nano 2025, 19, 9936−9945

alters Li (de)insertion pathways and strain/stress fields remain underexplored. Furthermore, the influence of cycling history on subsequent Li (de)insertion pathways is often overlooked.

Observing dynamic Li transport pathways associated with in situ-generated, electrochemically active nanocrack remains technically challenging. Recent advances, such as *operando* Bragg coherent X-ray diffraction imaging (BCDI), have enabled the observation of significant strain evolution, particularly [003] strain, within layered oxide particles ($Li_{1.2}Ni_{0.133}Mn_{0.533}Co_{0.133}O_2$) during charging.[25] However, the impact of Li transport pathways and the dynamic, nonhomogeneous distribution of Li on these evolving strain fields has not been explored. Additionally, *operando* optical microscopy has successfully visualized cracking phenomena in micrometer-sized anode particles, demonstrating that non-equilibrium phase separation induces particle cracking.[1] Yet, due to insufficient chemical and spatial resolution, this technique primarily captures large, major cracks that delaminate grains from particles, leaving electrochemically active nanocracks undetected. Other methods, such as four-dimensional scanning transmission electron microscopy and X-ray spectroptychography, have linked nanoscale Li composition and local strain in $LiFePO_4$ (LFP).[26] However, these observations were conducted under fully relaxed equilibrium conditions, failing to capture the dynamic nature of real-time battery operation.

Soft X-ray absorption-based in situ imaging is well-suited for visualizing Li transport pathways within battery nanoparticles and detecting the creation and evolution of nanocracks. Soft X-ray microscopy offers precise measurement of Li concentrations in nanoparticles with high chemical sensitivity, particularly when measuring L-edge absorption through selection-rule-allowed 2p-to-3d transitions.[27−29] This technique provides strong signal contrast even for battery particles as thin as 100 nm. In contrast, hard X-ray microscopy struggles to visualize nanocracks due to its low X-ray absorption contrast. For example, less than 1% of a hard X-ray probe is absorbed by 100 nm thick LFP particles, compared to 50% absorption for soft X-rays.[30,31] Consequently, hard X-ray microscopy has been limited to 5−10 μm sample size, which is too large to represent a single LFP particle, obscuring intraparticle nanocracks in two-dimensional projection images. Therefore, we propose that tracking the generation and evolution of nanocracks is ideally achieved using soft X-ray microscopy, though its strong absorption makes visualizing intraparticle Li transport in liquid electrochemical cells technically challenging.

RESULTS AND DISCUSSION

Redirection of Li Transport Pathways Driven by Nanocrack Formation. We developed *operando* scanning transmission X-ray microscopy (STXM) with high chemical sensitivity and spatial resolution to investigate how nanocracks influence dynamic Li transport pathways (Figure 1A, Supporting Note 1, and Figure S1). For this study, we prepared well-faceted, [100]-oriented, platelet-shaped LFP particles, both with and without nanocracks[30] (Figures S1 and S2). The nanofocused soft X-ray probe used in STXM raster-scanned the particles at a 45 nm pixel size, allowing for the acquisition of quantitative Li concentration maps. Each image pixel captured the transmission X-ray absorption spectra at the Fe L_3 edge. By fitting the pixel-wise absorption spectra to the linear combination of the end phase spectra of $Li_1Fe^{2+}PO_4$ and $Li_0Fe^{3+}PO_4$, we quantified the Fe-oxidation states and the lithium fraction, Li_xFePO_4 (Figure 1B). Through *operando* STXM, we imaged dynamic Li (de)insertion pathways within LFP particles.

LFP, a representative phase-separating material, garners significant attention due to its low manufacturing cost, which supports the expansion of the electric vehicle market. However, it suffers from considerable crack formation during cycling, driven by the large stresses induced by misfit strains between Li-rich and Li-poor phases.[8] To clearly observe crack formation and correlate it with Li (de)insertion pathways and their associated strain/stress fields, we designed a [100]-oriented LFP (~500 nm wide, ~1 μ m long, and ~150 nm thick). By positioning individual particles on a flat current collector of a microfabricated battery, we leveraged the flat (100) plane to visualize both the [010] diffusion channels and the (010) side-edge (de)insertion surfaces. The liquid electrochemical cells were constructed by sandwiching two SiN_x window chips, with the individual LFP particles placed on the thin, patterned carbon working electrode of one SiN_x chip. Ionic connections to the external Li metal reference/counter electrodes were established through microfluidic electrolyte channels, ensuring robust battery electrochemistry, consistent with our previous report[30] (Figure S1). To successfully observe Li transport pathways even after nanocrack formation during electrochemical cycling, we significantly improved particle-chip contacts by simultaneously carbonizing both the current collector and active particles[30,31] (Supporting Note 1 and Figure S3). This method allowed us to track electrochemically active nanocracks, which had previously been inaccessible.

Figure 1C,D illustrate the real-time evolution of Li concentration in both cracked and noncracked LFP particles. We conducted *operando* STXM on the noncracked LFP (Figure S4), which is consistent with our previous study,[30] particularly with cycling the as-synthesized particles during the initial cycle (Figures S5 and S6). The in situ lithium maps in Figure 1C are reproduced from our earlier reports for consistency. We note that Li-ion insertion and extraction initiated from the (010) side-edge surface of the noncracked LFP particles during discharging and charging, respectively.[30] As lithium inserts at both side edges, the Li-rich surface phases shrink along the [001] direction, inducing tensile stress in the middle of the particle and generates a crack along the [001] direction, which will be discussed later. This precycling (4 cycles of 0.2C charging/discharging) of pristine LFP on the microfabricated battery allows us to prepare cracked LFP particles (Figure S7), which were directly imaged via operando STXM (Figure 1D) using a separate chip from that used for the noncracked LFP experiment. Figure 1D clearly shows that the cracked surface substantially facilitates Li (de)insertion significantly more than the (010) side edge, with Li-ion insertion and extraction primarily occurring at the cracked-core region during lithiation and delithiation, respectively. This crack-mediated Li transport was observed across various C-rates (0.15 to 6C; Figure S8), supporting that the newly exposed cracked surfaces exhibit substantially higher (de)-insertion activity compared to the side-edge surfaces. Post-mortem scanning electron microscopy (SEM) of the same particles used for *operando* STXM (Figure 1E) confirmed that the crack locations coincided with the (de)lithiation hotspots, indicating that crack-initiated surface Li (de)insertion altered the overall Li transport pathways and the dynamic stress field within the particle.

https://doi.org/10.1021/acsnano.4c15960
ACS Nano 2025, 19, 9936−9945

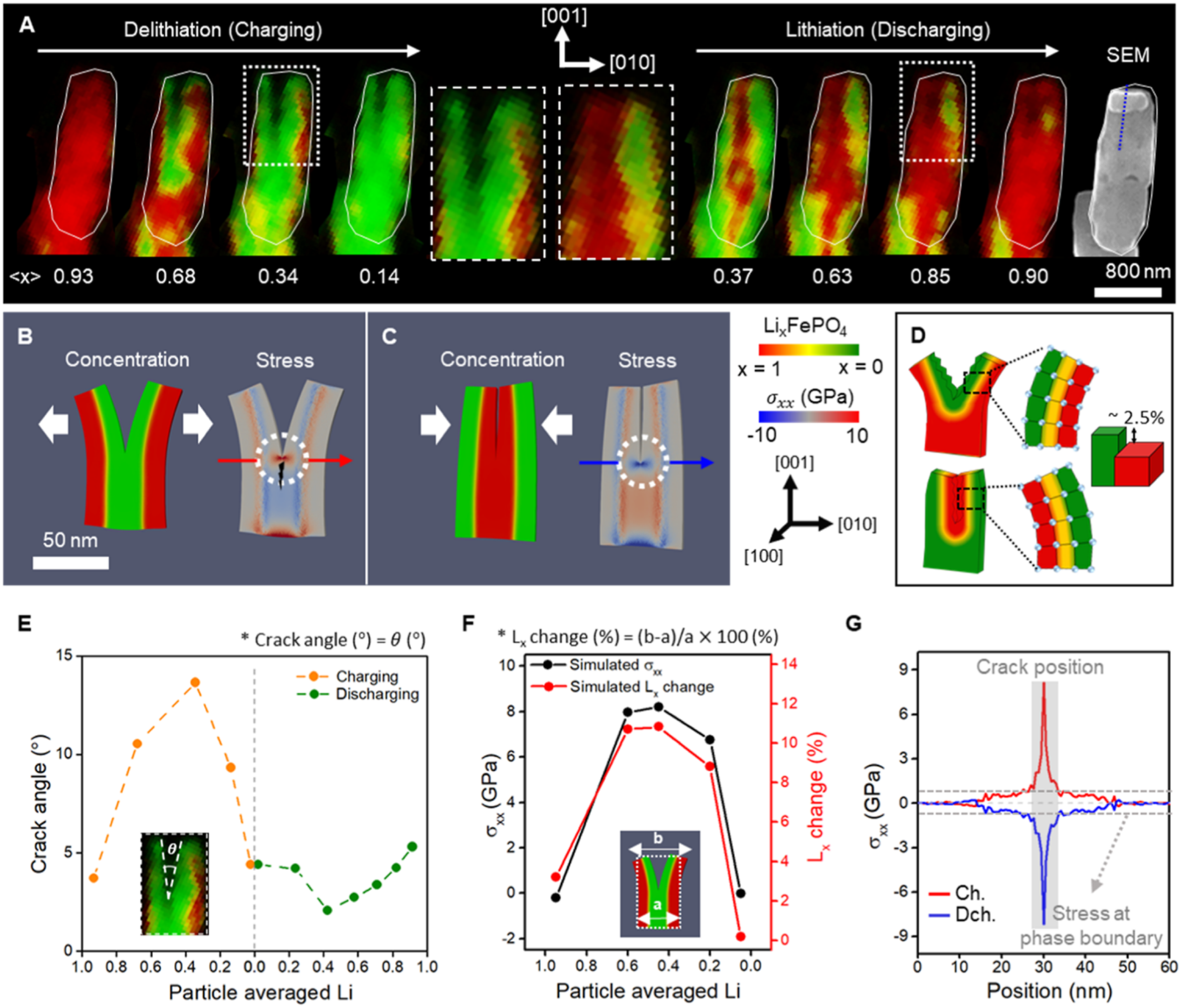

Figure 2. Chemo-mechanical stress evolved within cracked LFP particles accompanied by crack-opening and -closing. (A) Representative STXM images of a cracked LFP particle captured during charge and discharge and correlated SEM image. (B) Chemo-mechanical stress maps ([010]-direction eigen-stress, σ_{xx}) corresponding to the Li compositions, calculated by 3D phase-field simulations during charge and (C) discharge. (D) Schematic illustration of crack opening and closing. (E) Magnitude of crack opening angles captured from (A). (F) Calculated σ_{xx} and L_x changes during the charging process (the definition of L_x change is described above the graph (F)). (G) Line-cut profiles of σ_{xx} across the particle along the red and blue arrow in (B).

To compare (de)lithiation activity between the cracked surfaces and the original (010) side-edge surfaces in cracked LFP particles, we quantified the Li concentration at each pixel in the *operando* STXM images during cycling for seven particles (Figures 1F and S9–S11). The (010) side-edge pixels were designated as the original insertion surface, while cracked pixels in the middle of the particles, confirmed via correlative post-mortem SEM, were classified as cracked surfaces. During both delithiation and lithiation, the cracked surfaces showed faster changes in Li concentration compared with the side-edge surfaces, indicating enhanced (de)lithiation activity at the cracks (Figure 1G). This phenomenon persists even at high C-rates; however, at higher C-rates, the activity difference between the cracked surface and the original side-edge surface decreases (Figure S12). This can be interpreted as a mechanism to maximize the activation of the available active surfaces under high current densities.[30]

Chemo-Mechanical Stress Evolved within Cracked LFP Particles Resulting in Crack-Opening and -Closing. Our *operando* STXM on cracked LFP particles further revealed dynamic morphological changes resulting from the formation of fully split cracks, particularly near the cracked surfaces (Figures 2A–D and S13). As expected, (de)lithiation occurs faster near the cracks compared to other areas within the particle. During delithiation, Li-poor domains form along the crack while the side edges of the particle remain Li-rich from $\langle x \rangle \sim 0.68$ to $\langle x \rangle \sim 0.34$, where $\langle x \rangle$ represents the average Li concentration of the particle. Conversely, during lithiation, Li-rich domains develop along the crack while the side edges stay Li-poor from $\langle x \rangle \sim 0.37$ to 0.63. As a result, the crack located near the upper part of the particle opens during

https://doi.org/10.1021/acsnano.4c15960
ACS Nano 2025, 19, 9936–9945

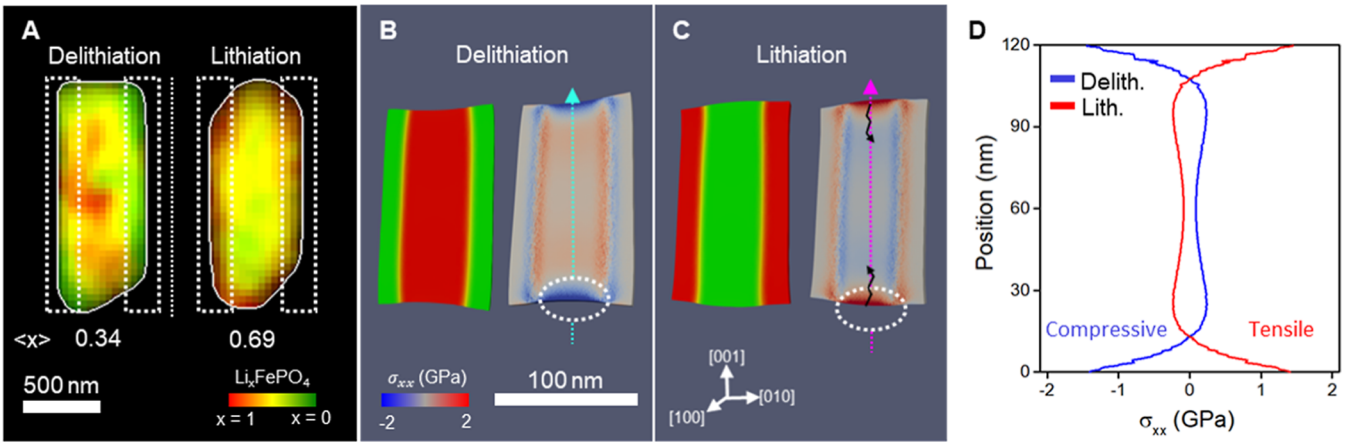

Figure 3. Chemo-mechanical stress evolved within noncracked LFP particles. (A) Representative STXM images of noncracked LFP particles captured during the charge and discharge process. Reproduced with permission from ref 30. Copyright 2023 Royal Society of Chemistry. (B) σ_{xx} maps corresponding to the Li compositions calculated by phase-field modeling during delithiation and (C) lithiation. (D) Line-cut profiles of σ_{xx} along the cyan and magenta arrows in (B) and (C), from the delithiation and lithiation simulation, respectively.

delithiation and closes during lithiation. The extent of crack opening and closing is reflected in the changing angle at the crack tip, measured from STXM images (Figure 2E). This fully split crack is clearly visible in the STXM image, starting with an initial crack angle of 3°. During delithiation, the angle increases significantly to 10° at $<x> \sim 0.4$, then reversibly decreases to 4° upon full delithiation. In contrast, during lithiation, the angle decreases further to 2° at $< x> \sim 0.4$, then reversibly increases back to around 5° at full lithiation. This behavior indicates that the crack alters the Li (de)insertion pathway, drives transient Li distribution around the crack, and modifies the local strain fields within the particle, revealing a chemo-mechanical deformation mechanism.

The driving force behind crack opening is illustrated in the simplified diagrams in Figure 2D. The extended misfit strain along the [001]-axis of the Li-poor phase causes the core region to expand in the [001] direction, while the particle edge, rich in lithium, remains shorter during charging.[32] During discharging, the reverse occurs, leading to crack closure. Notably, crack opening and closing are a reversible process, chemo-mechanically governed by the spatial distribution of Li-rich and Li-poor phases. We found no evidence that this reversible crack opening and closing causes immediate material deformation. As the charging and discharging processes near completion, the Li concentration within the particles becomes more uniform. Once the fully (de)lithiated state is reached, the stress caused by Li concentration gradients dissipates, and the particle regains its original morphology. This observation further indicates that ionic and electrical contact between the particles and the current collector remains intact throughout the cracking process.

To understand the evolution of the stress field associated with Li concentration distribution during crack opening and closing, we performed 3D phase-field simulations (Figures 2B,C,F,G, Supporting Information 2 and Figure S14). These simulations simultaneously calculate both Li concentration distribution and the corresponding stress field.[33−35] The 3D simulation is particularly suited for capturing the strong anisotropic properties of LFP. During charging, a Li-poor phase forms around the internal crack, while a Li-rich phase accumulates near the particle boundary (Figure 2B). This Li distribution generates significant tensile stress along the [010] direction (σ_{xx}), leading to crack opening. The stress at the crack tip, marked by a white circle in Figure 2B, is an order of magnitude greater (~1 GPa) than the interfacial stress at the LFP phase boundary[34] (Figure 2G), suggesting that the crack-mediated delithiation induces much larger deformation forces than expected from the typical biphasic interfacial stress.[4] In contrast, during discharging, compressive stress develops along the [010] direction (Figure 2C), resulting in crack closure. The magnitude of stress at the crack tip remains comparable to the charging process but with reversed direction (Figure 2G).

Our analysis of the evolved stress field during charging and discharging suggests that the direction of stress is critical in determining crack development. Specifically, tensile stress acts as the primary driving force for crack formation and development, potentially leading to particle splitting.[36] As established in prior studies,[37] the tensile stress perpendicular to the crack plane (mode I in fracture mechanics) is the dominant force behind crack propagation. This is supported by our simulation results (Figure 2F), which show that the extent of crack widening is directly proportional to the tensile stress at the crack tip. This tensile stress not only propagates the crack but also creates new active surface areas, altering the Li transport pathway. As a result, a recursive interaction is established between the redirections of the Li transport and the corresponding chemo-mechanical stress evolutions.

Chemo-Mechanical Stress Evolved within Non-cracked LFP Particles. As observed in the analysis of cracked LFP particles, the internal lithium distribution plays a critical role in determining the stress distribution. Consequently, tensile stress in noncracked LFP particles is also expected when a Li-poor phase develops in the core region, similar to cracked LFP particles (Figure 3A, reproduced from a previous report[30]). To confirm the occurrence of tensile stress and whether it is sufficient to induce cracking, phase-field simulations were performed on noncracked LFP particles, where (de)lithiation is initiated from the original (010) insertion boundary (Figure 3B). During discharging, a Li-rich phase evolved at the particle edges (the original (010) side-edge surfaces), while a Li-poor phase persisted in the core. This phase distribution is consistent with our STXM observations in noncracked LFP particles during discharging (Figure 3A). The contraction of the boundary region along the

https://doi.org/10.1021/acsnano.4c15960
ACS Nano 2025, 19, 9936−9945

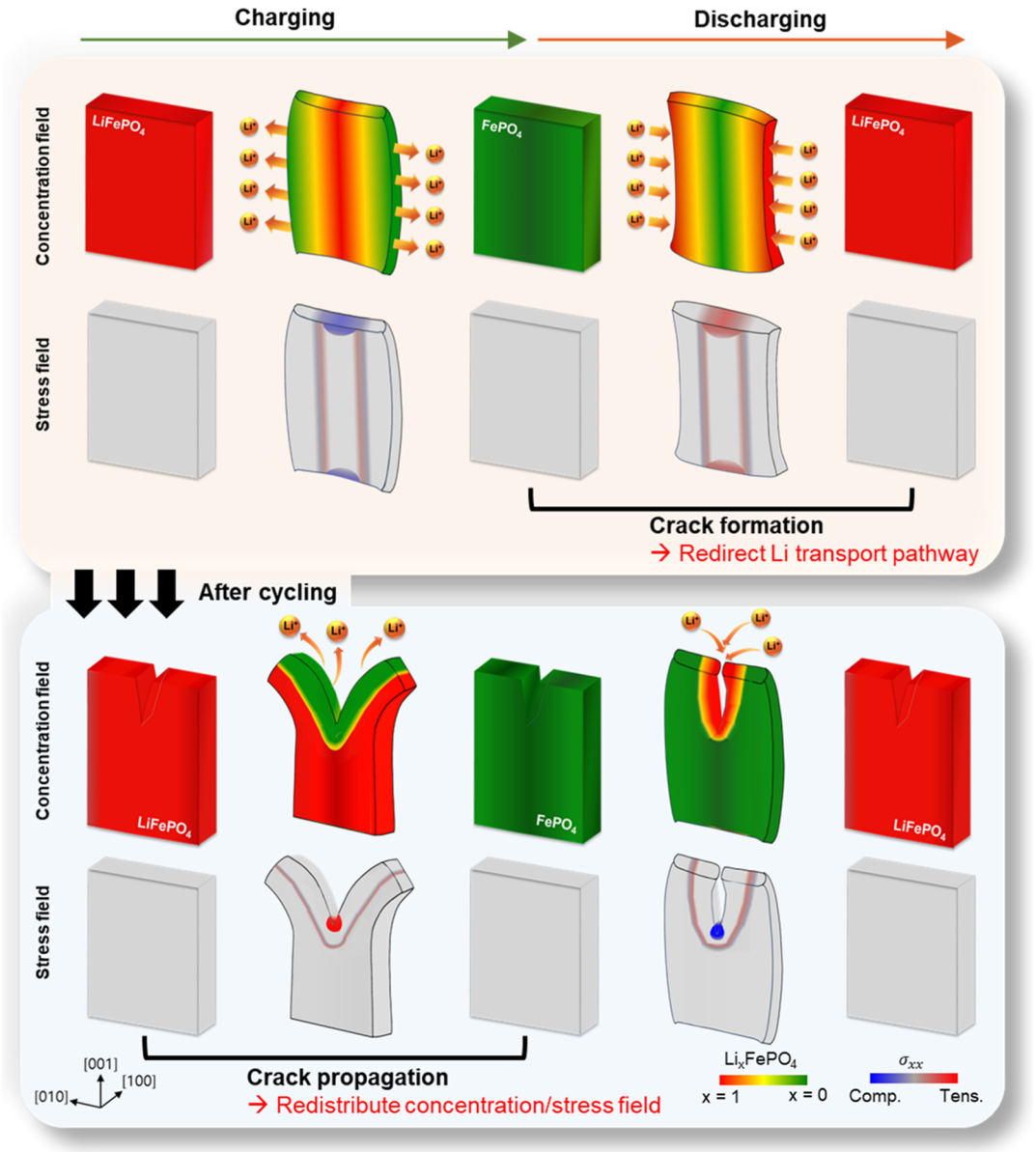

Figure 4. Chemo-mechanically coupled cracking pathway of LFP particles. During the charge and discharge of noncracked LFP, Li extraction and insertion primarily occur from the original (010) side-edge surfaces. The Li-rich phase formed at the (010) side edge during discharge, along with the Li-poor phase in the core region, generates tensile stress and may lead to crack formation. This redirects the lithium transport pathway. Cracked LFP initiates charge and discharge from the cracked surface. Tensile stress forms at the crack tip, correlating with the Li-poor phase formed at the cracked-core region during charging, facilitating crack propagation and redistributing the concentration and stress field within the particles. This chemo-mechanically interactive loop accelerates crack formation.

[001]-axis, in comparison to the core, generates strong tensile stress along the [010] direction, especially at the (001) surfaces located at the particle's top-bottom edges (Figure 3C). Our phase-field simulation suggests that this tensile stress is greater than that of the conventional biphasic interface and is likely sufficient to initiate crack formation within the LFP particles. Conversely, during the charging process, a Li-rich phase forms in the core region, inducing compressive stress and further supporting the correlation between the intra-particle lithium distribution and the direction of stress.

The combined *operando* STXM imaging and phase field simulation analysis demonstrates that, in many cases, the generated tensile stress can be more significant than previously expected at the interphase boundary (Figure 3D), depending on the phase distribution within LFP particles, specifically, the Li-rich shell and Li-poor core configuration. Based on these experimental and theoretical insights, we propose that noncracked particles are more prone to cracking during the discharge process and that this cracking is exacerbated during charging.

Li Concentration Distribution and Correlative Stress Field Determine Chemo-Mechanical Degradation Pathways in LFP Particles. Li concentration distribution and the resulting stress fields are key determinants of chemo-mechanical degradation in LFP particles. Using *operando* STXM imaging, we observed that cracks significantly alter the dynamic Li transport pathways. Phase-field simulations further demonstrated that the stress fields are closely linked to Li concentration distribution. Figure 4 illustrates the chemo-mechanical degradation pathways, showing how Li-rich and Li-

https://doi.org/10.1021/acsnano.4c15960
ACS Nano 2025, 19, 9936−9945

poor regions are shaped by the Li (de)insertion pathway and the correlated stress distribution. In noncracked LFP, Li extraction and insertion occur mainly along the (010) side edges, creating Li-poor and Li-rich phases during charging and discharging, respectively. During discharging, tensile stress at the (001) top and bottom edges—due to deformation along the *c*-axis relative to local Li concentration—promotes crack formation, while charging induces compressive stress at the same locations, corresponding to the inverse Li phase distribution.

Postcycling, cracks form and redirect the Li transport pathway, with delithiation and lithiation starting and expanding from the cracked-core regions during charging and discharging, respectively. As a result, the phase distribution in cracked LFP during charging resembles that of noncracked LFP during discharging, leading to tensile forces that propagate cracks, as observed in this study. During discharging, a Li-rich phase forms at the cracked core, generating compressive forces at the crack tip, which help to close the crack. This cyclical process accelerates chemo-mechanical degradation by continuously altering the crack size and increasing the active surface area. This is further supported by coin-cell experiments that quantify the number of cracked particles and the extent of crack propagation using SEM imaging, conducted on both [100]-oriented LFP and spherical-shaped commercial LFP (Figures S15 and S16), ultimately leading to reduced battery performance over time.

CONCLUSIONS

In this study, we clearly observed that crack formation significantly redirects dynamic Li transport pathways and revealed crack development mechanisms in individual LFP particles using operando STXM imaging. We hypothesize that the observed high reactivity of the cracked surface for Li (de)insertion, even in the absence of carbon coating, is related to high-energy surface exposure[38,39] and the sharpness of the cracked surface[31] (Figure S17). Additionally, we captured "crack-opening" during charging as direct evidence of crack propagation, driven by substantial chemo-mechanical tensile stress due to the distribution of Li-rich and Li-poor phase. The Li-rich and Li-poor phase distributions, obtained through *operando* STXM imaging with and without cracks, enabled accurate calculations in our 3D phase-field simulations. These simulations indicate that the tensile stress magnitude at the crack tip exceeds that at the biphasic interfaces, a detail not captured by *operando* STXM imaging. This promotes further crack development and supports a recursive loop involving Li transport pathways, crack development, and strain/stress fields (Movie S1).

These findings underscore the importance of differentiating the chemo-mechanics of active materials before and after crack formations. They also highlight the need for *operando* studies that investigate dynamic Li concentration distributions alongside strain, stress, and crack formation. Our results suggest that crack formation could be suppressed by controlling particle shape,[40−42] surface doping, or coating[43,44] to minimize the tensile forces caused by Li concentration gradients. Specifically, surface coatings and doping can reduce the surface-to-core chemical gradient by making Li-poor or Li-rich phases either favorable or unfavorable on the surface or in the core.[45]

Additionally, optimizing charge−discharge protocols by modulating current density can further reduce crack formation.[30,31] For example, when charging and discharging occur within the same time frame, high-rate charging in the initial cycles could help suppress crack initiation, while high-rate discharging in later cycles could inhibit crack propagation (Figures S18−S20). This also supports the idea that crack formation does not occur only at the phase boundary but can also happen away from the boundary (off-boundary) due to tensile stress resulting from the Li transport pathway and the distribution of Li-rich/Li-poor phases (Figure S21). Furthermore, with recent advancements toward higher energy densities,[46] there is a growing interest in using larger single crystals of LFP. While larger particle sizes are typically associated with poor rate capabilities, an alternative strategy could involve intentionally inducing initial cracks to create additional active surface area and reduce diffusion lengths, thereby improving rate performance.

Beyond LFP, heterogeneous Li concentration and phase distributions are frequently observed during cycling in various solid-solution materials.[1,47−49] Uneven phase evolution in these materials can also lead to localized stresses and structural deformations, resulting in cracks that potentially redirect Li transport pathways. Understanding these phenomena can contribute positively to the design of active materials and cycling protocols aimed at inhibiting capacity fading due to crack formation, ultimately enhancing the longevity of LIBs.

MATERIALS AND METHODS

Synthesis. The Li_3PO_4, which is a precursor for LFP synthesis, can be synthesized by the acid and alkali neutralization reaction between H_3PO_4 (ACS reagent, ≥85 wt % in H_2O, Sigma Aldrich) and $LiOH{\cdot}H_2O$ (98%, Alfa Aesar). A lithium hydroxide solution with a Li^+ concentration of 0.5 M was initially prepared by dissolving $LiOH{\cdot}H_2O$ in 100 mL of deionized water. Subsequently, 0.673 mL of H_3PO_4 (85% solution) was added dropwise over 5 min into the solution under magnetic stirring, forming a white suspension. After magnetic stirring at room temperature for an additional 15 min, the resultant suspension underwent centrifugation using 50 mL conical tubes, followed by multiple washes with deionized water. The purified product was then dried at 110 °C for 12 h. The obtained Li_3PO_4 was stored in a desiccator for subsequent experiments. Furthermore, $FeSO_4{\cdot}7H_2O$ (≥99%, Sigma Aldrich) powders were heated at 100 °C for 12 h in a vacuum oven to obtain dried form.

A solvothermal method was utilized for the synthesis of [100]-oriented $LiFePO_4$ (LFP) particles with previously prepared Li_3PO_4, $FeSO_4$ powders, and H_3PO_4 (85% solution) as starting materials. Specifically, Li_3PO_4 (0.4304 g, 3.717 mmol) was introduced into a cosolvent containing 2.5 mL of ethylene glycol (anhydrous, 99.8%, Sigma Aldrich) and 2.5 mL of deionized water in a 50 mL Teflon liner under magnetic stirring at room temperature. Subsequently, 0.126 mL of H_3PO_4 was added to the suspension, followed by the sequential addition of $FeSO_4$ (0.5646 g, 3.717 mmol) and ascorbic acid (≥99%, Sigma Aldrich, 0.019 g, 0.108 mmol) to achieve a molar ratio of Li/Fe/P = 3:1:1.5. After sealing in a hydrothermal reactor, the autoclave was heated in a convection oven up to 180 °C and held for 2 h, and the resulting suspension was filtered through a porous membrane filter (pore size: 0.45 μm), washed with deionized water four times and with anhydrous ethanol 1 time, and dried at 110 °C for 12 h.

Scanning Transmission X-Ray Microscopy (STXM). *Operando* and ex situ STXM experiments were conducted at the beamline of 10ID-1 at the Canadian Light Source (CLS), 10A1 at Pohang Accelerator Laboratory (PAL), and MYSTIIC at BESSY II Helmholtz Zentrum Berlin. Fe L_3-edge absorption near ∼710 eV was measured during experiments. Images were raster scanned in 45 nm steps, and the oxidation state of Fe was quantified by linear combination using reference spectra of $Fe^{3+}PO_4$ and $LiFe^{2+}PO_4$.

SEM. SEM images were obtained by an Apreo 2S with a 15 kV acceleration voltage and a 0.4 nA current.

https://doi.org/10.1021/acsnano.4c15960
ACS Nano 2025, 19, 9936−9945

Phase-Field Simulation. The phase-field simulation utilized in this study uses a Cahn−Hilliard-type equation incorporating diffusional chemical potential. In order to address chemo-mechanical internal stress, an elastic chemical potential term with coherency strain was introduced. Assuming the absence of external forces acting on the particle, we set the divergence of the elastic stress tensor to zero. These governing equations were discretized via the finite element method, solved by python code utilizing the FEniCS library.

ASSOCIATED CONTENT

Data Availability Statement

All data generated and analyzed are included in the paper and its Supporting Information. All custom codes to conduct simulations that are reported in this manuscript are available from the corresponding author upon reasonable request.

Supporting Information

The Supporting Information is available free of charge at https://pubs.acs.org/doi/10.1021/acsnano.4c15960.

Chemo-mechanically coupled recursive cracking pathway of LFP particles (MP4)

Operando STXM platform description and electrochemistry using a microfluidic cell, model particle validation using SEM, XRD, and TEM, chip preparation method and validation using SEM, additional representative operando STXM images and analysis, description of the 3D phase-field model simulation, SEM and statistical analysis of crack-suppressing cycling protocols, and schematic representation of the LFP cracking process (PDF)

AUTHOR INFORMATION

Corresponding Author

Jongwoo Lim − *Department of Chemistry, Seoul National University, Seoul 08826, Republic of Korea; Institute of Applied Physics and Institute for Battery Research Innovation, Seoul National University, Seoul 08826, Republic of Korea;* orcid.org/0000-0002-3897-7488; Email: jwlim@snu.ac.kr

Authors

Chihyun Nam − *Department of Chemistry, Seoul National University, Seoul 08826, Republic of Korea*

Bonho Koo − *Department of Chemistry, Seoul National University, Seoul 08826, Republic of Korea;* Present Address: Leiden Institute of Chemistry, Leiden University, Leiden, The Netherlands; orcid.org/0000-0003-1637-689X

Juwon Kim − *Department of Chemistry, Seoul National University, Seoul 08826, Republic of Korea*

Jinkyu Chung − *Department of Chemistry, Seoul National University, Seoul 08826, Republic of Korea;* orcid.org/0000-0001-7809-7912

Jaejung Song − *Department of Chemistry, Seoul National University, Seoul 08826, Republic of Korea*

Danwon Lee − *Department of Chemistry, Seoul National University, Seoul 08826, Republic of Korea*

Sungjae Seo − *Department of Chemistry, Seoul National University, Seoul 08826, Republic of Korea*

Munsoo Song − *Department of Chemistry, Seoul National University, Seoul 08826, Republic of Korea*

Seyeon Shin − *Department of Chemistry, Seoul National University, Seoul 08826, Republic of Korea*

Namdong Kim − *Pohang Accelerator Laboratory, Pohang University of Science and Technology, Pohang, Gyeongbuk 37673, South Korea;* orcid.org/0000-0002-9615-2863

Markus Weigand − *Helmholtz-Zentrum Berlin (HZB), Berlin 12489, Germany*

Jian Wang − *Canadian Light Source Inc., Saskatoon, Saskatchewan S7N 2 V3, Canada;* orcid.org/0000-0001-5184-7023

Complete contact information is available at: https://pubs.acs.org/10.1021/acsnano.4c15960

Author Contributions

¶C.N., B.K., and J.K. are co-first authors and contributed equally to this work. C. N. and B. K. analyzed the overall STXM data and wrote the manuscript. C. N. developed 3D phase field simulation with B. K. B. K., J. K., and J. C. conducted *operando* STXM experiments with assistance from J. W. C. N., D. L., S.J., M. W., and N. K supported *operando* and ex-situ STXM experiments. J. K., C. N., and J. J. synthesized [100]-oriented platelet LFP single. SEM images were conducted by C. N. and J. J. M. S. and S. S. contributed to crucial discussions. J. L. supervised this work. All authors contributed to the discussion of the results.

Notes

The authors declare no competing financial interest.

ACKNOWLEDGMENTS

This work is supported by the National Research Foundation of Korea (NRF) grant funded by the Korea government (MSIT) (RS-2023-00261543, RS-2024-00347008, and RS-2023-00247245). Chihyun Nam is supported by the Basic Science Research Program through the National Research Foundation of Korea (NRF) funded by the Ministry of Education (RS-2024-00412069). Bonho Koo acknowledges the support by the Basic Science Research Program through the National Research Foundation of Korea (NRF) funded by the Ministry of Education (RS-2024-00412310).

REFERENCES

(1) Merryweather, A. J.; Jacquet, Q.; Emge, S. P.; Schnedermann, C.; Rao, A.; Grey, C. P. Operando Monitoring of Single-Particle Kinetic State-of-Charge Heterogeneities and Cracking in High-Rate Li-Ion Anodes. *Nat. Mater.* **2022**, *21* (11), 1306−1313.

(2) Liu, T.; Liu, J.; Li, L.; Yu, L.; Diao, J.; Zhou, T.; Li, S.; Dai, A.; Zhao, W.; Xu, S.; Ren, Y.; Wang, L.; Wu, T.; Qi, R.; Xiao, Y.; Zheng, J.; Cha, W.; Harder, R.; Robinson, I.; Wen, J.; Lu, J.; Pan, F.; Amine, K. Origin of Structural Degradation in Li-Rich Layered Oxide Cathode. *Nature* **2022**, *606* (7913), 305−312.

(3) Pistorio, F.; Clerici, D.; Mocera, F.; Somà, A. Review on the Experimental Characterization of Fracture in Active Material for Lithium-Ion Batteries. *Energies* **2022**, *15* (23), 9168.

(4) Fu, J.; Wang, K.; Liu, D.; Zhang, Z.; Sui, M.; Yan, P. B. Axis Phase Boundary Movement Induced (020) Plane Cracking in $LiFePO_4$. *ACS Appl. Mater. Interfaces* **2020**, *12* (35), 39245−39251.

(5) Cheng, Y.-T.; Verbrugge, M. W. Diffusion-Induced Stress, Interfacial Charge Transfer, and Criteria for Avoiding Crack Initiation of Electrode Particles. *J. Electrochem. Soc.* **2010**, *157* (4), A508.

(6) Kondrakov, A. O.; Schmidt, A.; Xu, J.; Geßwein, H.; Mönig, R.; Hartmann, P.; Sommer, H.; Brezesinski, T.; Janek, J. Anisotropic Lattice Strain and Mechanical Degradation of High- and Low-Nickel NCM Cathode Materials for Li-Ion Batteries. *J. Phys. Chem. C* **2017**, *121* (6), 3286−3294.

(7) Seok, J.; Lee, W.; Lee, H.; Park, S.; Chung, C.; Hwang, S.; Yoon, W.-S. Aging Mechanisms of Lithium-Ion Batteries. *J. Electrochem. Sci. Technol.* **2024**, *15* (1), 51−66.
(8) Chen, G.; Song, X.; Richardson, T. J. Electron Microscopy Study of the $LiFePO_4$ to $FePO_4$ Phase Transition. *Electrochem. Solid-State Lett.* **2006**, *9* (6), A295.
(9) Scipioni, R.; Jørgensen, P. S.; Hjelm, J.; Norby, P.; Rasmussen, C. N.; Jensen, S. H. Degradation Studies on $LiFePO_4$ Cathode. *ECS Trans.* **2015**, *64* (22), 97.
(10) Lim, J. M.; Hwang, T.; Kim, D.; Park, M. S.; Cho, K.; Cho, M. Intrinsic Origins of Crack Generation in Ni-Rich $LiNi_{0.8}Co_{0.1}Mn_{0.1}O_2$ Layered Oxide Cathode Material. *Sci. Rep.* **2017**, *7*, 2−11.
(11) Li, T.; Yuan, X.-Z.; Zhang, L.; Song, D.; Shi, K.; Bock, C. Degradation Mechanisms and Mitigation Strategies of Nickel-Rich NMC-Based Lithium-Ion Batteries. *Electrochem. Energy Rev.* **2020**, *3* (1), 43−80.
(12) Wang, D.; Wu, X.; Wang, Z.; Chen, L. Cracking Causing Cyclic Instability of $LiFePO_4$ Cathode Material. *J. Power Sources* **2005**, *140* (1), 125−128.
(13) Gabrisch, H.; Wilcox, J.; Doeff, M. M. TEM Study of Fracturing in Spherical and Plate-like $LiFePO_4$ Particles. *Electrochem. Solid-State Lett.* **2008**, *11* (3), A25.
(14) Meng, X.-H.; Lin, T.; Mao, H.; Shi, J.-L.; Sheng, H.; Zou, Y.-G.; Fan, M.; Jiang, K.; Xiao, R.-J.; Xiao, D.; Gu, L.; Wan, L.-J.; Guo, Y.-G. Kinetic Origin of Planar Gliding in Single-Crystalline Ni-Rich Cathodes. *J. Am. Chem. Soc.* **2022**, *144* (25), 11338−11347.
(15) Yan, P.; Zheng, J.; Gu, M.; Xiao, J.; Zhang, J.-G.; Wang, C.-M. Intragranular Cracking as a Critical Barrier for High-Voltage Usage of Layer-Structured Cathode for Lithium-Ion Batteries. *Nat. Commun.* **2017**, *8* (1), 14101.
(16) Christensen, J.; Newman, J. Stress Generation and Fracture in Lithium Insertion Materials. *J. Solid State Electrochem.* **2006**, *10* (5), 293−319.
(17) Xu, T.; Wu, J.; Ding, J.; Huang, Y.; Huang, Y.; Zhao, W. Advancements in Addressing Microcrack Formation in Ni−Rich Layered Oxide Cathodes for Lithium−Ion Batteries. *ChemElectroChem* **2024**, *11* (12), No. e202300802.
(18) Heenan, T. M. M.; Wade, A.; Tan, C.; Parker, J. E.; Matras, D.; Leach, A. S.; Robinson, J. B.; Llewellyn, A.; Dimitrijevic, A.; Jervis, R.; Quinn, P. D.; Brett, D. J. L.; Shearing, P. R. Identifying the Origins of Microstructural Defects Such as Cracking within Ni-Rich NMC811 Cathode Particles for Lithium-Ion Batteries. *Adv. Energy Mater.* **2020**, *10* (47), 2002655.
(19) Barai, P.; Rojas, T.; Narayanan, B.; Ngo, A. T.; Curtiss, L. A.; Srinivasan, V. Investigation of Delamination-Induced Performance Decay at the Cathode/LLZO Interface. *Chem. Mater.* **2021**, *33* (14), 5527−5541.
(20) Park, K.-J.; Hwang, J.-Y.; Ryu, H.-H.; Maglia, F.; Kim, S.-J.; Lamp, P.; Yoon, C. S.; Sun, Y.-K. Degradation Mechanism of Ni-Enriched NCA Cathode for Lithium Batteries: Are Microcracks Really Critical? *ACS Energy Lett.* **2019**, *4* (6), 1394−1400.
(21) Nam, G. W.; Park, N.-Y.; Park, K.-J.; Yang, J.; Liu, J.; Yoon, C. S.; Sun, Y.-K. Capacity Fading of Ni-Rich NCA Cathodes: Effect of Microcracking Extent. *ACS Energy Lett.* **2019**, *4* (12), 2995−3001.
(22) Trevisanello, E.; Ruess, R.; Conforto, G.; Richter, F. H.; Janek, J. Polycrystalline and Single Crystalline NCM Cathode Materials—Quantifying Particle Cracking, Active Surface Area, and Lithium Diffusion. *Adv. Energy Mater.* **2021**, *11* (18), 2003400.
(23) Gao, T.; Kim, A.; Lu, W. Modeling Electrode-Level Crack and Quantifying Its Effect on Battery Performance and Impedance. *Electrochim. Acta* **2020**, *363*, 137197.
(24) Min, J.; Gubow, L. M.; Hargrave, R. J.; Siegel, J. B.; Li, Y. Direct Measurements of Size-Independent Lithium Diffusion and Reaction Times in Individual Polycrystalline Battery Particles. *Energy Environ. Sci.* **2023**, *16* (9), 3847−3859.
(25) Singer, A.; Zhang, M.; Hy, S.; Cela, D.; Fang, C.; Wynn, T. A.; Qiu, B.; Xia, Y.; Liu, Z.; Ulvestad, A.; Hua, N.; Wingert, J.; Liu, H.; Sprung, M.; Zozulya, A. V.; Maxey, E.; Harder, R.; Meng, Y. S.; Shpyrko, O. G. Nucleation of Dislocations and Their Dynamics in Layered Oxide Cathode Materials during Battery Charging. *Nat. Energy* **2018**, *3* (8), 641−647.
(26) Deng, H. D.; Zhao, H.; Jin, N.; Hughes, L.; Savitzky, B. H.; Ophus, C.; Fraggedakis, D.; Borbély, A.; Yu, Y.-S.; Lomeli, E. G.; Yan, R.; Liu, J.; Shapiro, D. A.; Cai, W.; Bazant, M. Z.; Minor, A. M.; Chueh, W. C. Correlative Image Learning of Chemo-Mechanics in Phase-Transforming Solids. *Nat. Mater.* **2022**, *21* (5), 547−554.
(27) Kim, J.; Lee, S. Y.; Kim, S.-J.; Koo, B.; Chung, J.; Lee, D.; Choi, S.; Kim, J.; Seo, S.; Nam, C.; Gandionco, K. A.; Bak, G.; Jo, S.; Kim, N.; Shin, H.-J.; Chae, K. H.; Won, D. H.; Marcus, M. A.; Shapiro, D. A.; Haw, S.-C.; Alsem, D. H.; Salmon, N. J.; Min, B. K.; Kim, H.; Hwang, Y. J.; Lim, J. Spatiotemporal Active Phase Evolution for CO_2 Electrocatalysis. *Joule* **2024**, *8* (12), 3373−3385.
(28) Chung, J.; Nam, C.; Kim, J. Y.; Lee, T. H.; Kim, J.; Lee, D.; Koo, B.; Jo, S.; Cho, J.; Kunze, S.; Choi, Y. S.; Song, J.; Choi, H.; Kim, J.; Park, S. H.; Lee, H.; Hong, B. H.; Kim, N.; Shapiro, D. A.; Jang, H. W.; Lim, J. Elucidating Heterogeneous Li Insertion Using Single-Crystalline and Freestanding Layered Oxide Thin Film. *Nano Lett.* **2024**, *24* (46), 14766−14773.
(29) Kim, J.; Lee, D.; Nam, C.; Chung, J.; Koo, B.; Kim, N.; Lim, J. Energy Material Analysis via In-Situ/Operando Scanning Transmission x-Ray Microscopy: A Review. *J. Electron Spectrosc. Relat. Phenom.* **2023**, *266*, 147337.
(30) Koo, B.; Chung, J.; Kim, J.; Fraggedakis, D.; Seo, S.; Nam, C.; Lee, D.; Han, J.; Jo, S.; Zhao, H.; Nadkarni, N.; Wang, J.; Kim, N.; Weigand, M.; Bazant, M. Z.; Lim, J. Dynamic Surface Phases Controlling Asymmetry of High-Rate Lithiation and Delithiation in Phase-Separating Electrodes. *Energy Environ. Sci.* **2023**, *16* (8), 3302−3313.
(31) Lim, J.; Li, Y.; Alsem, D. H.; So, H.; Lee, S. C.; Bai, P.; Cogswell, D. A.; Liu, X.; Jin, N.; Yu, Y.; Salmon, N. J.; Shapiro, D. A.; Bazant, M. Z.; Tyliszczak, T.; Chueh, W. C. Origin and Hysteresis of Lithium Compositional Spatiodynamics within Battery Primary Particles. *Science* **2016**, *353* (6299), 566−571.
(32) Wang, L.; Zhou, F.; Meng, Y. S.; Ceder, G. First-Principles Study of Surface Properties of $LiFePO_4$: Surface Energy, Structure, Wulff Shape, and Surface Redox Potential. *Phys. Rev. B* **2007**, *76* (16), 165435.
(33) ChiuHuang, C.-K.; Huang, H.-Y. S. Critical Lithiation for C-Rate Dependent Mechanical Stresses in $LiFePO_4$. *J. Solid State Electrochem.* **2015**, *19* (8), 2245−2253.
(34) Yang, K.; Tang, M. Three-Dimensional Phase Evolution and Stress-Induced Non-Uniform Li Intercalation Behavior in Lithium Iron Phosphate. *J. Mater. Chem. A* **2020**, *8* (6), 3060−3070.
(35) Fleck, M.; Federmann, H.; Pogorelov, E. Phase-Field Modeling of Li-Insertion Kinetics in Single $LiFePO_4$-Nano-Particles for Rechargeable Li-Ion Battery Application. *Comput. Mater. Sci.* **2018**, *153*, 288−296.
(36) Lajtai, E. Z. A Theoretical and Experimental Evaluation of the Griffith Theory of Brittle Fracture. *Tectonophysics* **1971**, *11* (2), 129−156.
(37) Richard, H. A.; Kuna, M. Theoretical and Experimental Study of Superimposed Fracture Modes I, II and III. *Eng. Fract. Mech.* **1990**, *35* (6), 949−960.
(38) Gu, J.; Chen, H.; Shi, Y.; Cao, Z.; Du, Z.; Li, B.; Yang, S. Eliminating Lightning-Rod Effect of Lithium Anodes via Sine-Wave Analogous MXene Layers. *Adv. Energy Mater.* **2022**, *12* (36), 2201181.
(39) Geldasa, F. T.; Kebede, M. A.; Shura, M. W.; Hone, F. G. Identifying Surface Degradation, Mechanical Failure, and Thermal Instability Phenomena of High Energy Density Ni-Rich NCM Cathode Materials for Lithium-Ion Batteries: A Review. *RSC Adv.* **2022**, *12* (10), 5891−5909.
(40) Stamps, M. A.; Eischen, J. W.; Huang, H. Y. S. Particle- and Crack-Size Dependency of Lithium-Ion Battery Materials $LiFePO_4$. *AIMS Mater. Sci.* **2016**, *3* (1), 190−203.
(41) Cogswell, D. A.; Bazant, M. Z. Size-Dependent Phase Morphologies in $LiFePO_4$ Battery Particles. *Electrochem. Commun.* **2018**, *95*, 33−37.

https://doi.org/10.1021/acsnano.4c15960
ACS Nano 2025, 19, 9936−9945

(42) Shahid, R.; Murugavel, S. Particle Size Dependent Confinement and Lattice Strain Effects in $LiFePO_4$. *Phys. Chem. Chem. Phys.* **2013**, *15* (43), 18809−18814.
(43) Wang, D.; Li, H.; Shi, S.; Huang, X.; Chen, L. Improving the Rate Performance of $LiFePO_4$ by Fe-Site Doping. *Electrochim. Acta* **2005**, *50* (14), 2955−2958.
(44) Pei, B.; Wang, Q.; Zhang, W.; Yang, Z.; Chen, M. Enhanced Performance of $LiFePO_4$ through Hydrothermal Synthesis Coupled with Carbon Coating and Cupric Ion Doping. *Electrochim. Acta* **2011**, *56* (16), 5667−5672.
(45) Qian, G.; Huang, H.; Hou, F.; Wang, W.; Wang, Y.; Lin, J.; Lee, S.-J.; Yan, H.; Chu, Y. S.; Pianetta, P.; Huang, X.; Ma, Z.-F.; Li, L.; Liu, Y. Selective Dopant Segregation Modulates Mesoscale Reaction Kinetics in Layered Transition Metal Oxide. *Nano Energy* **2021**, *84*, 105926.
(46) Syed, M. A.; Salehabadi, M.; Obrovac, M. N. High Energy Density Large Particle $LiFePO_4$. *Chem. Mater.* **2024**, *36* (2), 803−814.
(47) Xu, C.; Merryweather, A. J.; Pandurangi, S. S.; Lun, Z.; Hall, D. S.; Deshpande, V. S.; Fleck, N. A.; Schnedermann, C.; Rao, A.; Grey, C. P. Operando Visualization of Kinetically Induced Lithium Heterogeneities in Single-Particle Layered Ni-Rich Cathodes. *Joule* **2022**, *6* (11), 2535−2546.
(48) Merryweather, A. J.; Schnedermann, C.; Jacquet, Q.; Grey, C. P.; Rao, A. Operando Optical Tracking of Single-Particle Ion Dynamics in Batteries. *Nature* **2021**, *594* (7864), 522−528.
(49) Lee, E.; Lee, D.-H.; Bessette, S.; Park, S.-W.; Brodusch, N.; Lazaris, G.; Kim, H.; Malik, R.; Gauvin, R.; Seo, D.-H.; Lee, J. Nearly All-Active-Material Cathodes Free of Nickel and Cobalt for Li-Ion Batteries. *Energy Environ. Sci.* **2024**, *17* (11), 3753−3764.

https://doi.org/10.1021/acsnano.4c15960
ACS Nano 2025, 19, 9936−9945